Adaptive Dealiasing for Doppler Velocities Scanned from Hurricanes and Typhoons

YUAN JIANG

National Meteorological Center, China Meteorological Administration, and State Key Laboratory of Severe Weather, Chinese Academy of Meteorological Sciences, Beijing, China

QIN XU

NOAA/National Severe Storms Laboratory, Norman, Oklahoma

(Manuscript received 9 July 2015, in final form 9 May 2016)

ABSTRACT

By fitting a parametric vortex model directly to aliased radar radial velocities scanned from a hurricane, the maximum tangential velocity and its radial distance from the hurricane vortex center can be estimated by the recently developed alias-robust vortex analysis. This vortex analysis can be refined to produce a suitable reference radial velocity field on each tilt of a radar scan for the reference check in the first main step of dealiasing. This paper presents the techniques developed for the refinements and shows how and to what extent the refined vortex analysis can improve the reference check and thus enhance the dealiased data coverage, especially over severely aliased data areas around the vortex core of a hurricane or typhoon. In addition, stringent threshold conditions are used in the reference check and the subsequent continuity check to ensure the accepted data are free of alias or almost so. The robustness and improved performance of the method are exemplified by the results tested with severely aliased radial velocities scanned by operational WSR-88D radars from hurricanes in the United States and by operational China New Generation Weather Radar (CINRAD) base data format SA radars from typhoons in China.

1. Introduction

It is well known in radar meteorology that there is a maximum velocity, called the Nyquist velocity and denoted by v_N, beyond which the radial velocities measured by a Doppler radar are aliased by an integer multiplied by the Nyquist velocity back into the Nyquist interval between $\pm v_N$ (Doviak and Zrnić 2006, section 3.6). Such an integer is called the Nyquist folding number, and it can be either positive or negative. The central task in correcting an aliased velocity is to determine the Nyquist folding number. This task, called dealiasing, can be accomplished if the alias can be detected and corrected by comparing the aliased radial velocity (i) with a reference radial velocity and/or (ii) with radial velocities measured by the same radar at the neighborhood data points for their continuities in space (or in space and time). These two types of comparisons, called the reference check and the continuity check, respectively, have been commonly used in combinations, but their applications are often confronted with difficulties caused by the absence of any reliable reference velocity and by the lack of a correctly dealiased velocity to start the checking.

The Nyquist velocities used by operational weather radars in the United States are usually in the range between 20 and 36 $m s^{-1}$, so radial velocities scanned from a hurricane can easily exceed these Nyquist velocities and become severely aliased. The operationally used dealiasing techniques (Eilts and Smith 1990; Jing and Wiener 1993; Witt et al. 2009) for processing real-time WSR-88D radar data were developed primarily for visual and certain quantitative applications with considerable tolerance for bad or poor-quality data to retain as much as possible the original data coverage. The processed data often do not satisfy the high-quality standard required by radar data assimilation. This problem is not completely solved by the dealiasing techniques so far developed, and difficulties are

Corresponding author address: Dr. Qin Xu, National Severe Storms Laboratory, 120 David L. Boren Blvd., Norman, OK 73072-7326.
E-mail: qin.xu@noaa.gov

DOI: 10.1175/JTECH-D-15-0146.1

often encountered that are sometimes insurmountable due to the lack of reliable reference information about the true wind field. The encountered difficulties have been reduced to a certain extent by modifying the velocity–azimuth display (VAD) analysis (Browning and Wexler 1968) for direct applications to raw radial velocities to provide reference winds for dealiasing (Yamada and Chong 1999; Tabary et al. 2001; Haase and Landelius 2004; Gong et al. 2003; Gao et al. 2004; Zhu and Gong 2006, Xu et al. 2011). In particular, by formulating the aliasing-caused zigzag discontinuities into the cost function for the VAD fitting via the unconventional approach based on the Bayesian estimation theory (Xu 2009), an alias-robust VAD (AR-VAD) analysis was developed by Xu et al. (2010, hereafter X10) to estimate the mean horizontal wind directly from raw aliased radial velocity data. This AR-VAD analysis was used to produce a reference radial velocity field for radar velocity dealiasing in the first main step of the AR-VAD-based dealiasing method (Xu et al. 2011, hereafter X11). The AR-VAD-based dealiasing has been used operationally for radar data assimilation applications at the National Centers of Environmental Prediction (NCEP) in the United States (Liu et al. 2009). To satisfy the high-quality standard required by operational data assimilation, stringent threshold conditions have been used in the AR-VAD-based dealiasing to ensure the accepted data are free of alias, but good data are also sometimes rejected in areas where the true wind field becomes too nonuniform to satisfy the VAD uniform-wind approximation. This has limited the dealiased data coverage, as often seen from hurricane (or typhoon) winds scanned by operational radars.

Because aliasing can occur in countless different ways and the aliasing scenarios can be extremely complex, it is very difficult or even impossible to develop a single dealiasing method for all different and difficult scenarios to satisfy the high-quality standard required by radar data assimilation. To overcome the difficulties, efforts have been made in developing various adaptive dealiasing methods (rather than a single method) beyond the AR-VAD-based dealiasing. One of the outcomes from these efforts is the adaptive dealiasing (Xu and Nai 2012) based on the alias-robust variational (AR-Var) analysis (Xu and Nai 2013), which was designed specifically for severe winter ice storms scanned by WSR-88D radars using the volume coverage pattern 31 (VCP31) with the Nyquist velocity reduced below $12\,\mathrm{m\,s^{-1}}$. Computationally, this adaptive dealiasing is marginally efficient for operational radar data assimilation applications because each VCP31 volume contains only five tilts of raw radial velocities scanned in about 10 min. As shown by Xu et al. (2013, hereafter X13), the AR-Var-based dealiasing can be further extended and used in place of the AR-VAD-based dealiasing for scan modes other than VCP31, but the required computational time is increased significantly. The extended AR-Var-based dealiasing is thus not sufficiently efficient for operational radar data assimilation applications, especially for assimilating hurricane winds scanned by using VCP21 (VCP121), because each VCP21 (VCP121) volume contains 19 tilts of raw radial velocities scanned in no more than 5 min. Thus, as another outcome from the aforementioned efforts, a new efficient dealiasing is developed adaptively for hurricanes or typhoons by refining the alias-robust (AR) vortex analysis of Xu et al. (2014, hereafter XJL) and using it in place of the AR-VAD analysis for the reference check in the first main step of the AR-VAD-based dealiasing.

The performance of the new adaptive dealiasing was highlighted in XJL by an example without presenting the detailed techniques, because the involved refinements are complicated by partially unphysical needs for dealiasing (as explained later in section 2d) and thus not suitable for other possible applications of the AR vortex analysis. Since the detailed techniques are not published but critical for dealiasing, this paper aims to present the detailed dealiasing techniques and show how and to what extent the refined vortex analysis can improve dealiasing adaptively, especially over severely aliased data areas around the vortex core of a hurricane or typhoon. The new adaptive dealiasing has been tested with severely aliased radial velocities (497 volumes) scanned by operational China New Generation Weather Radar (CINRAD) base data format SA radars from typhoons in China in addition to those listed in XJL that were scanned by operational WSR-88D radars from hurricanes in the United States. According to these tests, the new method not only improves the accepted data coverage over the core area of a hurricane or typhoon but also ensures the accepted data are free of alias or almost so. The paper is organized as follows. The refinements made to the AR vortex analysis for dealiasing are presented in the next section. The new method is presented in section 3 with illustrative examples to show the robustness and improved performance of the method. Conclusions follow in section 4. Variables and symbols listed and defined in the appendix will be used in the paper directly without further explanation.

2. Refined AR vortex analysis for dealiasing

Images of radar-observed radial velocity v_r^{obs} from a hurricane or typhoon often exhibit a narrow near-zero-v_r^{obs} zone [see the zigzag gray stripe marked by the yellow + sign in Fig. 5a] containing the true (nonaliased and unobserved) zero-v_r line between the radar and

vortex center on each tilt of radar scan. As the image pixel moves away from this near-zero-v_r^{obs} zone, the raw v_r^{obs} often becomes aliased quickly and severely. Because of this, it is necessary and critical to accurately estimate the true zero-v_r line on each tilt and use it to constrain the AR vortex analysis so the analysis-produced reference radial velocity v_r^{ref} can be sufficiently accurate for dealiasing, especially on the two sides of the true zero-v_r line on each tilt. To achieve this, the AR vortex analysis presented in sections 2–4 of XJL needs to be refined with complex logic in three key components. The detailed logic steps in these three key components are presented in three subsections after the parametric vortex model and related properties are briefly reviewed in the following subsection.

a. Parametric vortex model and zero-v_r point ϕ_+

As shown in XJL, the parametric vortex of Vatistas et al. (1991) can be used to describe the tangential wind V_T of a hurricane as a function of the radial distance R from the hurricane vortex center at each vertical level in the following form (see Fig. 1 in XJL):

$$V_T = V_M(R/R_M)[1/2 + (R/R_M)^4/2]^{-1/2}, \tag{1}$$

where V_M is the maximum tangential velocity at $R = R_M$. The hurricane vortex center location (r_c, ϕ_c), in the radar-centered coordinates (see Fig. 2 in XJL), can be pre-estimated from operationally issued hurricane location information. The environmental mean wind is usually much smaller than V_M, and it impacts mostly the asymmetric flow retrieval but not much the axisymmetric flow according to Murillo et al. (2011) and Harasti et al. (2004). Thus, the environmental mean wind can be neglected. According to (1), v_r can be modeled by

$$v_r^{mod} = V_T \sin(\alpha - \phi)\cos\theta', \tag{2}$$

where α, ϕ, and θ' are defined in the appendix. The expression in (2) will be used not only to fit v_r^{obs} for the refined vortex analysis in the next subsection but also to compute v_r^{ref} for the reference check in the first main step of dealiasing in section 3a.

Note that R and α are functions of (r, ϕ, r_c, ϕ_c) determined by the cosine and sine formulas in (4b) and (4c) of XJL, respectively. Substituting the latter two equations into (1) and then into (2) gives the modeled v_r in the form of

$$v_r^{mod} = A[1 + (R/R_M)^4]^{-1/2}\sin(\phi - \phi_c), \tag{3}$$

where $A = (2^{1/2}V_M r_c/R_M)\cos\theta'$. For fixed r_c, ϕ_c, V_M, R_M, and θ, A is constant and R is a function of ϕ, so v_r^{mod} is also a function of ϕ according to (3). Since $A > 0$ and $R \geq 0$, it is easy to see from (3) that $v_r^{mod}(\phi)$ changes sign twice on a range circle at two zero-v_r points:

$$\phi = \phi_+ = \phi_c \tag{4a}$$

and

$$\phi = \phi_- = \phi_+ + 180° - 360°\,\mathrm{Int}[(\phi_+ + 180°)/360°], \tag{4b}$$

where Int[( )] represents the nearest integer of ( ), ϕ_+ (ϕ_-) denotes the zero-v_r point associated with $\partial_\phi v_r^{mod} > 0$ ($\partial_\phi v_r^{mod} < 0$). The last term in (4b) is just for the purpose of keeping ϕ_- in the same period as ϕ_+, say, between $-180°$ and 180°.

Note that ϕ_+ (ϕ_-) is the nearest point to (farthest point from) the vortex center among all the points on a range circle; that is, $\mathrm{Min}R(\phi) = R(\phi_+) = |r_c - r|$ and $\mathrm{Max}R(\phi) = R(\phi_-) = r_c + r$. Applying ∂_ϕ to (4b) in XJL and (3) gives

$$\partial_\phi v_r^{mod} = (\pi/180°)A[1 + (R/R_M)^4]^{-1/2}[\cos(\phi - \phi_c) - 2rr_cR^2(R_M^4 + R^4)^{-1}\sin^2(\phi - \phi_c)], \tag{5a}$$

$$\mathrm{Max}[\partial_\phi v_r^{mod}(\phi)] = \partial_\phi v_r^{mod}(\phi_+) = (\pi/180°)A(1 + |r_c - r|^4 R_M^4)^{-1/2}, \tag{5b}$$

$$\mathrm{Min}[\partial_\phi v_r^{mod}(\phi)] = \partial_\phi v_r^{mod}(\phi_-) = -(\pi/180°)A[1 + (r_c + r)^4/R_M^4]^{-1/2}. \tag{5c}$$

Thus, $\partial_\phi v_r^{mod}$ reaches the positive (negative) maximum at ϕ_+ (ϕ_-) on a range circle, and the positive maximum of $\partial_\phi v_r^{mod}$ at ϕ_+ is larger or much larger than the absolute value of the negative maximum of $\partial_\phi v_r^{mod}$ at ϕ_-, especially when $|r_c - r| < R_M <$ or $< (r_c + r)$.

b. Search for ϕ_+ on each selected range circle

As explained in (1), ϕ_c can be pre-estimated by ϕ_c^{op} from operationally issued hurricane location information. According to (4a), ϕ_+ can be searched from the raw v_r^{obs} around ϕ_c^{op} on each selected range circle by using the following three properties. (i) There can be more than one $\phi^{obs}{}_0$ point (where $|v_r^{obs}|$ reaches a local minimum below 2 m s^{-1}) but only one $\phi^{obs}{}_+$ point (if it exists among $\phi^{obs}{}_0$ points) in the immediate vicinity of the true ϕ_+ point. (ii) Around $\phi^{obs}{}_+$, v_r^{true} is small and thus v_r^{obs} is free of alias, so the true ϕ_+ can be estimated by a local least squares fit to v_r^{obs} around $\phi^{obs}{}_+$. (iii) When the local least squares fit applies to v_r^{obs} around a $\phi^{obs}{}_0$ point other than $\phi^{obs}{}_+$, the associated $\partial_\phi v_r$ cannot be as large as that at $\phi^{obs}{}_+$ because the latter should be the largest

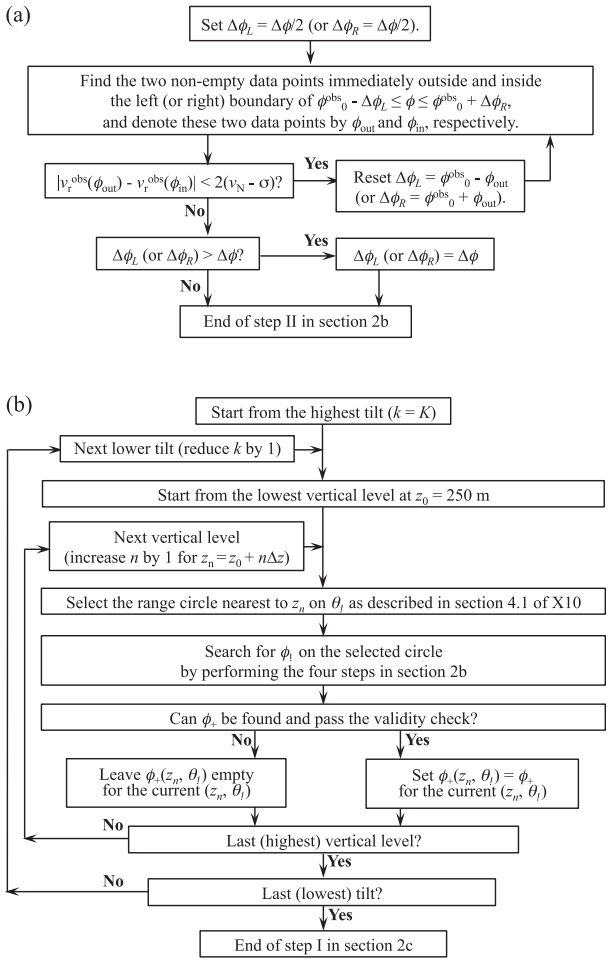

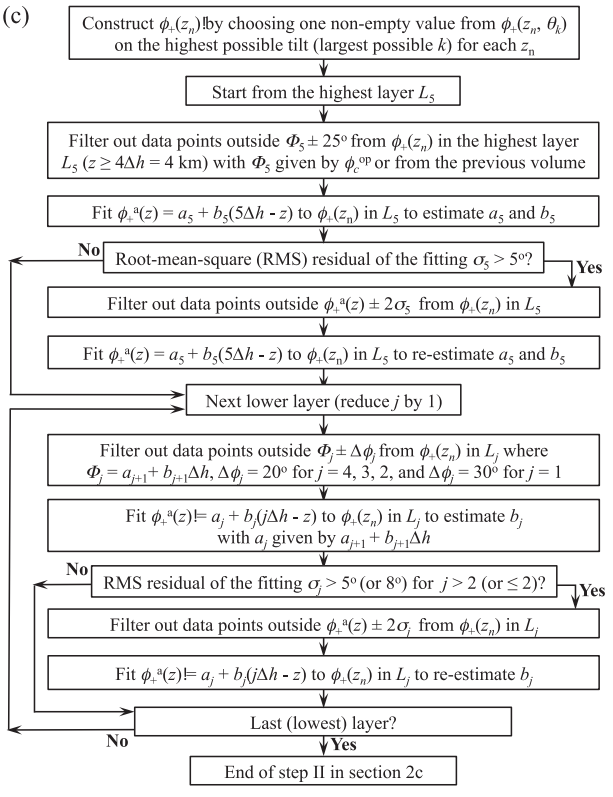

FIG. 1. Flowcharts for (a) step 2 in section 2b, (b) step 1 in section 2c, (c) step 2 in section 2c, and (d) step 3 in section 2c. In (a), σ (=2 m s^{-1}) is the standard deviation of the observation error (not including alias error).

FIG. 1. (*Continued*)

point as implied by (5b). This property allows $\phi^{obs}{}_+$ to be distinguished from all other $\phi^{obs}{}_0$ points.

The above-mentioned three properties are used to search for ϕ_+ on each selected range circle by performing the following four steps.

1) Search for $\phi^{obs}{}_0$ points within $\phi_c{}^{op} \pm 80°$ by performing step Ia in appendix A in X10. This search is more efficient than the search over the entire circle used in XJL.
2) Determine the left (right) half-window width $\Delta\phi_L$ ($\Delta\phi_R$) for each $\phi^{obs}{}_0$ by performing the continuity check counterclockwise (clockwise), as shown by the flowchart in Fig. 1a.
3) Find the local zero-v_r point and associated $\partial_\phi v_r$ around each $\phi^{obs}{}_0$ by applying the local least squares fit (described in step Ib of appendix A in X10) to $v_r{}^{obs}$ (must be eight or more nonempty data points) within $\phi^{obs}{}_0 - \Delta\phi_L \le \phi \le \phi^{obs}{}_0 + \Delta\phi_R$. Here, unlike step Ib in appendix A in X10, the half-window width is not set to $\Delta\phi$ because $v_r{}^{obs}$ is not always alias free within $\phi^{obs}{}_+ \pm \Delta\phi$.
4) Set ϕ_+ to the zero point that has the largest $\partial_\phi v_r$ among all the local zero points found above.

c. *Estimate ϕ_+ as a function of z on each tilt*

As explained at the beginning of section 2, it is necessary and critical to accurately estimate ϕ_+ as a function of z or essentially r from $v_r{}^{obs}$ on each tilt. This is accomplished by performing the following three steps.

1) Search for ϕ_+ on each range circle (selected nearest to each discrete vertical level along each tilt) and go through the entire volume to generate $\phi_+(z_n, \theta_k)$ as a discrete function of (z_n, θ_k), as shown by the flowchart in Fig. 1b.
2) Construct $\phi_+(z_n)$ from $\phi_+(z_n, \theta_k)$ and estimate $\phi_+{}^a(z)$ by recursively fitting a piecewise-linear continuous function form of $a_j + b_j(j\Delta h - z)$ to $\phi_+(z_n)$ in each vertical layer (from the highest to the lowest layer indexed by j = 5, 4, 3, 2, 1), as shown by the flowchart in Fig. 1c.
3) Estimate $\phi_+{}^a(z, \theta_k)$ by recursively fitting a piecewise-linear continuous function to $\phi_+(z_n, \theta_k)$ on each tilt through the entire volume, as shown by the flowchart in Fig. 1d.

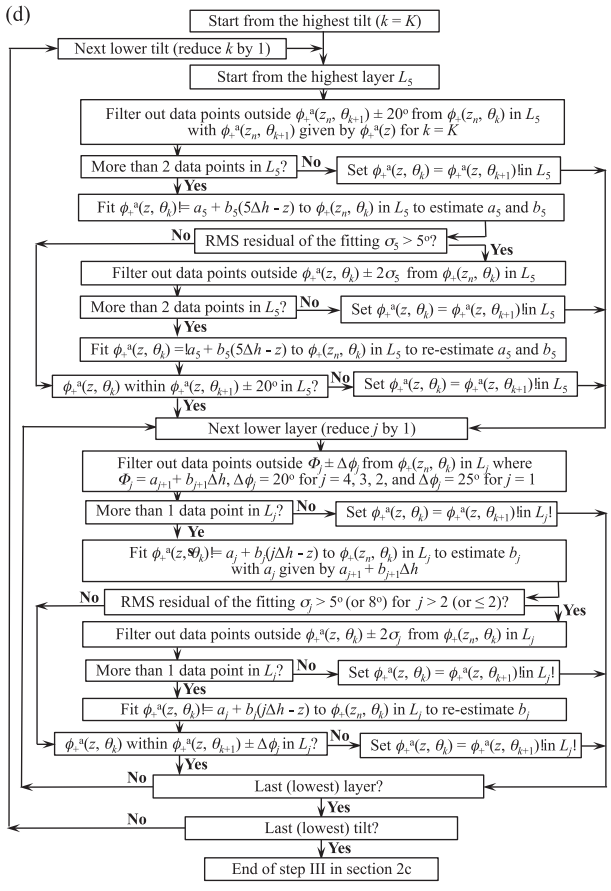

FIG. 1. (*Continued*)

As an example, the discrete vertical profile $\phi_+(z_n)$ constructed in step 2 is plotted by the plus and multiplication signs in Fig. 2a. As shown, this constructed $\phi_+(z_n)$ contains not only densely packed true zero-v_r points (plotted by blue + signs) but also scattered false zero-v_r points (plotted by red × signs). The false zero-v_r points are from severely aliased areas on the two sides of the true zero-v_r points, and they are occasionally selected by the searching algorithm (at the vertical levels of the red × signs) due to various reasons. The recursive fitting in step 2 is designed to filter out these false zero-v_r points and other possible outliers from $\phi_+(z_n)$ to enhance the accuracy of the estimated ${\phi_+}^a(z)$, as shown by the black solid line in Fig. 2a.

The discrete vertical profile $\phi_+(z_n, \theta_K)$ on the highest tilt of $\theta_K = \theta_{14} = 19.5°$ is plotted by the blue plus signs in Fig. 2b. As shown, there are just two data points in each of the lowest three layers (i.e., L_j for $j = 3, 2$, or 1), so the coefficient b_j in the fitting function $a_j + b_j(j\Delta h–z)$ can be still, but poorly, estimated from the two data points in L_j for $j = 3$, 2, or 1 by the initial fitting in step 2. However, the constructed ${\phi_+}^a(z, \theta_{14})$ at the lower boundary of L_j is not within $\pm\Delta\phi_j$ of ${\phi_+}^a(z)$ for j = 3, 2, or 1 (not shown), so the previously estimated b_j in step 2 is used here again to reconstruct ${\phi_+}^a(z, \theta_{14})$ in L_j for j = 3, 2, or 1, in step 3. This explains why the final estimated ${\phi_+}^a(z, \theta_K)$ (plotted by the black solid line in Fig. 2b) does not closely follow the sparse data points in the lowest three layers but follows the same slantwise pattern as ${\phi_+}^a(z)$ in Fig. 2a.

Figure 2c shows that the discrete vertical profile $\phi_+(z_n, \theta_2)$ is empty in L_5 and contains many false zero-v_r points in L_4–L_2. These false zero-v_r points are filtered out by the initial fitting in step 3, while ${\phi_+}^a(z, \theta_2)$ is constructed in the empty layer L_5 on θ_2 by the subsequent recursive fitting in step 3. This explains why and how ${\phi_+}^a(z, \theta_2)$ is estimated as a piecewise-linear continuous function over the entire vertical range, as shown by the black solid line in Fig. 2c. Figure 2d shows that the discrete vertical profile $\phi_+(z_n, \theta_1)$ is not only empty in L_5 but also very sparse with false zero-v_r points in L_4–L_1. Nevertheless, by performing the recursive fitting in step 3, ${\phi_+}^a(z, \theta_1)$ can be estimated over the entire vertical range, as shown by the black solid line in Fig. 2d.

d. Refined AR vortex analysis constrained by ${\phi_+}^a(z, \theta_k)$

As explained at the beginning of section 2, the above-estimated ${\phi_+}^a(z, \theta_k)$ should be used to constrain the AR vortex analysis. This is done by setting $\phi_c = {\phi_+}^a(z, \theta_k)$ as a refined estimate of ϕ_c (to replace the preestimated value ϕ_c^{op}) in the modified cost function [see (6)] for the refined AR vortex analysis at each vertical level. Physically, the variation of ϕ_+ with z (or r) on each tilt can be caused by many factors (especially the nonaxisymmetric and non-tangential flow structures neglected by the vortex model) in addition to the variation of ϕ_c with z—the only factor that can be considered here by setting $\phi_c = {\phi_+}^a(z, \theta_k)$. Because only the tangential velocity V_T is considered by the vortex model in (1)–(3), ϕ_+ cannot vary with z (r) on any tilt in the vortex model unless ϕ_c varies with z, and the variation of ϕ_+ with z (r) cannot match ${\phi_+}^a(z, \theta_k)$ on every tilt unless ϕ_c is set to ${\phi_+}^a(z, \theta_k)$ for the AR vortex analysis. This explains why we need to set $\phi_c = {\phi_+}^a(z, \theta_k)$ as a mathematical treatment that is partially unphysical. As shown in Figs. 9b and 9c in XJL, the AR vortex analysis and its estimated (V_M, R_M) are not sensitive to small or even finite errors in (r_c, ϕ_c), so setting $\phi_c = {\phi_+}^a(z, \theta_k)$ will not significantly deteriorate the physical realism of the estimated (V_M, R_M) but improve the accuracy of v_r^{ref} to ensure the reference check is free of false dealiasing, as explained earlier.

For the reference check in section 3a, v_r^{ref} must be adequately accurate (at least within $\pm 7v_N/4$ of v_r^{true} for the threshold value of $v_N/4$ used by the reference check) at every observation point to not deflag an aliased v_r^{obs} and thus avoid false dealiasing. Because of this, it is better to estimate (V_M, R_M) by using all available observations from all the range circles (one per tilt) around each selected vertical level, and this can also improve

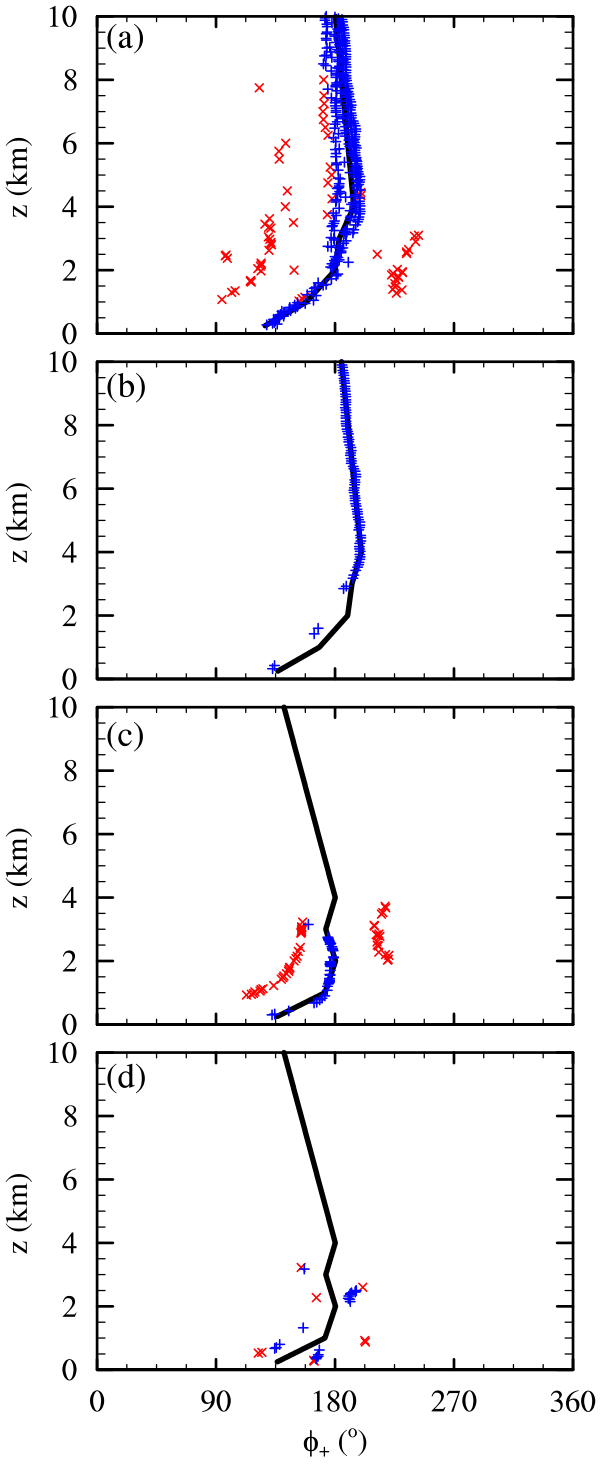

FIG. 2. (a) Discrete vertical profile $\phi_+(z_n)$ plotted by blue + signs for retained zero-v_r points and by red × signs for rejected zero-v_r points and estimated $\phi_+{}^a(z)$ plotted by the black solid line. (b) Discrete vertical profile $\phi_+(z_n, \theta_K)$ on the highest tilt ($\theta_K = \theta_{14} = 19.5°$) and estimated $\phi_+{}^a(z, \theta_K)$. (c) Discrete vertical profile $\phi_+(z_n, \theta_2)$ on the second lowest tilt ($\theta_2 = 1.45°$) and estimated $\phi_+{}^a(z, \theta_2)$. (d) Discrete vertical profile $\phi_+(z_n, \theta_1)$ on the lowest tilt ($\theta_1 = 0.5°$) and estimated $\phi_+{}^a(z, \theta_1)$. All the results are produced from a full volume of $v_r{}^{obs}$ scanned from Hurricane Katrina by the KLIX radar over the 5-min period from 1028 to 1033 UTC 29 Aug 2005.

the robustness of the estimated (V_M, R_M) to errors in (r_c, ϕ_c), as shown in section 4b in XJL. The cost function in (7) in XJL is thus modified into the following form:

$$J(V_M, R_M) = \sum_k \sum_i \{Z[v_r^{\text{mod}}(V_M, R_M, \phi_i, r_k) - v_r^{\text{obs}}(\phi_i, r_k), v_N]\}^2 / \sum_k m_k \quad \text{for} \quad z = z_n, \tag{6}$$

where $Z[(), v_N] \equiv () - 2v_N \text{Int}[()/(2v_N)]$ is the aliasing operator defined in (6) in XJL, $r_k = r(\theta_k)$ is the range radius of the kth circle selected from the kth tilt closest to the vertical level at $z = z_n$, $\sum_k$ denotes the summation over k from 1 to K (i.e., the number of the highest tilt θ_K), $\sum_i$ denotes the summation over i from 1 to m_k, and m_k is the total number of observations on the kth circle. In (6), $v_r{}^{\text{mod}}(V_M, R_M, \phi_i, r_k)$ is the radial velocity modeled by (3) in which R is a function of $(\phi_i, r_k, \phi_c, r_c)$ for $r = r_k$ and $\phi = \phi_i$, while ϕ_c is set to $\phi_+{}^a(z, \theta_k)$ and r_c is preestimated from operationally issued hurricane location information and will be fine-tuned as described later.

As shown by the black solid lines in Figs. 2b and 2c, the estimated $\phi_+{}^a(z, \theta_K)$ and $\phi_+{}^a(z, \theta_2)$ decrease rapidly as z decreases toward and into the boundary layer (below 1 km). This feature is seen for every estimated $\phi_+{}^a(z, \theta_k)$ and is caused by the strong inward radial wind in the hurricane boundary layer. Since the hurricane radial wind is not considered in the vortex model, the refined vortex analysis is not applicable to the hurricane boundary layer. Besides, the environmental mean wind can become significant in the middle and upper troposphere but is neglected in the vortex model, so the refined vortex analysis can become inaccurate as z increases to 4 km and beyond. Since the reference check does not have to produce seed data over the entire radial range (and thus the entire depth) on each tilt, it is safe and sufficient to apply the refined vortex analysis only to selected vertical levels between 1 km $\le z \le$ 4 km. Here, "seed data" are termed as those dealiased or deflagged good data that are produced and accepted by the reference check in the first main step and used as "seeds" by the continuity check in the second main step.

At each vertical level (every $\Delta z = 25$ m from $z = 1$ to 4 km), the global minimum of the cost function J in (6) can be searched in the space of (V_M, R_M) by using the standard conjugate gradient descent algorithm (see section 3 in XJL). To fine-tune r_c, we simply select a series of 17 uniformly distributed values for r_c (every 2.5 km apart) in the ±20-km vicinity of the preestimated r_c, and then find the global minimum, $J^{\min}(r_c) = J[V_M{}^{\min}(r_c), R_M{}^{\min}(r_c)]$, for each selected value of r_c, where $[V_M{}^{\min}(r_c), R_M{}^{\min}(r_c)]$ is the global minimum point for the selected r_c. Among the nine selected values of r_c, the value

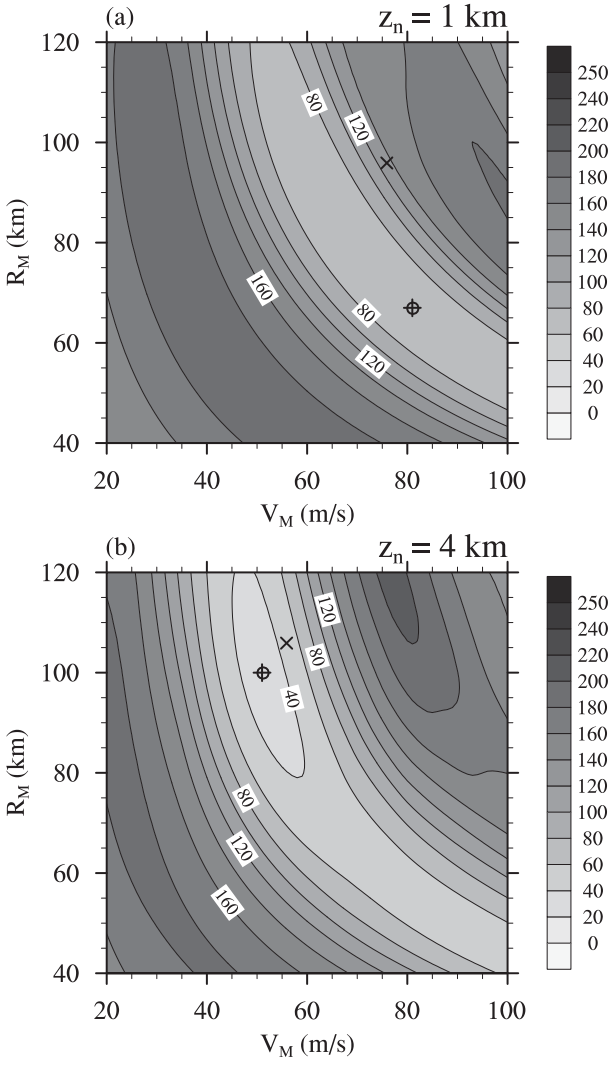

FIG. 3. Cost functions $J(V_M, R_M)$ for (a) $z_n = 1$ km and (b) $z_n = 4$ km in (6) computed by including all 14 circles of $v_r^{obs}(\phi_i, r_k)$ (on 14 tilts) from the same volume of v_r^{obs} as that used in Fig. 2. In each panel, the × sign marks the initial guess of (V_M, R_M) used by the descent algorithm, and the + sign marks the global minimum point found by the descent algorithm that is almost identical to the global minimum point (marked by the o sign) found by the brute-force search (with resolutions of 1 m s^{-1} in V_M and 1 km in R_M).

that yields the smallest $J^{min}(r_c)$ is used as a refined estimate of r_c at the selected vertical level z_n. This refined estimate is denoted by r_c^e, and $(V_M^e, R_M^e) = [V_M^{min}(r_c^e), R_M^{min}(r_c^e)]$ is the global minimum point for $r_c = r_c^e$.

As explained in section 3a in XJL, a suitable initial guess of (V_M, R_M) can be easily obtained from operationally issued hurricane wind information within the concave area of the cost function. This feature is shown by the example in Fig. 3a (Fig. 3b), where r_c is already fine-tuned to r_c^e = 179.16 km for z_n = 1 km (r_c^e = 164.16 km for z_n = 4 km) after ϕ_c is set to $\phi_+^a(z, \theta_k)$ for each range circle (selected on each tilt θ_k) around $z = z_n$ = 1 km (4 km). As shown in Fig. 3a (Fig. 3b), the initial guess (marked by the × sign) is at $(V_M, R_M) = (76\,\text{m s}^{-1}, 96\,\text{km})$ for z_n = 1 km [or $(V_M, R_M) = (56\,\text{m s}^{-1}, 106\,\text{km})$ for z_n = 4 km], while the global minimum point (V_M^e, R_M^e) found by the descent algorithm (marked by the + sign) is at $(V_M, R_M) = (81.09\,\text{m s}^{-1}, 66.91\,\text{km})$ for z_n = 1 km [or $(V_M, R_M) = (51.20\,\text{m s}^{-1}, 99.94\,\text{km})$ for z_n = 4 km], which is almost identical to the global minimum point (marked by the open circle) found by the brute-force search (with resolutions of 1 m s^{-1} in V_M and 1 km in R_M). The algorithm converges in 28 (12) iterations in Fig. 3a (Fig. 3b). Note that the concaved area of $J(V_M, R_M)$ is more elongated around the global minimum in Fig. 3a than in Fig. 3b, which largely explains why the convergence requires more iterations in Fig. 3a than in Fig. 3b. As the selected vertical level increases from z_n = 1 to 2 km and beyond, the geometry of $J(V_M, R_M)$ changes gradually and becomes very similar to that in Fig. 3b, so the required number of iteration decreases rapidly toward 12. The descent algorithm is thus not only accurate but also very efficient in most cases. This convergence property is similar to that found in XJL but is now further tested and verified with real radar radial velocities.

After r_c^e, V_M^e, and R_M^e are obtained for each vertical level as functions of z_n, they are treated as input data for the least squares fits to estimate $r_c^a(z)$, $V_M^a(z)$, and $R_M^a(z)$, respectively, as linear functions of z over the vertical range of 1 km ≤ z ≤ 4 km. The input $r_c^e(z_n)$, $V_M^e(z_n)$, and $R_M^e(z_n)$ are plotted with their estimated $r_c^a(z)$, $V_M^a(z)$, and $R_M^a(z)$ in Figs. 4a–c, respectively, for the same radar volume scan as that used in Figs. 2 and 3. Figure 4a shows that $r_c^a(z)$ decreases linearly from 178.6 to 155.6 km as z increases from 1 to 4 km, and this linear decrease fits the general trend of the variation of $r_c^e(z_n)$ with z_n, although the data points of $r_c^e(z_n)$ become increasingly scattered as z_n increases above 2.5 km. The decrease of $r_c^a(z)$ with z in Fig. 4a may imply that the hurricane vortex center is slanted toward the radar site as z increases (from 1 to 4 km). However, because of the highly nonlinear dependence of J on r_c and the simplicity of the vortex model, the refined estimate r_c^e may not necessarily always be a more accurate estimate than the preestimated r_c (independent of z). Nevertheless, among the 17 selected values of r_c, r_c^e yields the best fit of $v_r^{mod}(V_M, R_M, \phi_i, r_k)$ to $v_r^{obs}(\phi_i, r_k)$ measured by $J^{min}(r_c)$, and this property is important as it is just what we need for dealiasing, regardless of the accuracy or inaccuracy of r_c^e estimated as a function of height. Figure 4b shows that $V_M^a(z)$ decreases linearly from 66.3 to 49.7 m s^{-1} as z increases from 1 to 4 km, and this linear decrease fits $V_M^e(z_n)$ closely. Figure 4c shows that $R_M^a(z)$ increases linearly from 84 to 105 km, and this

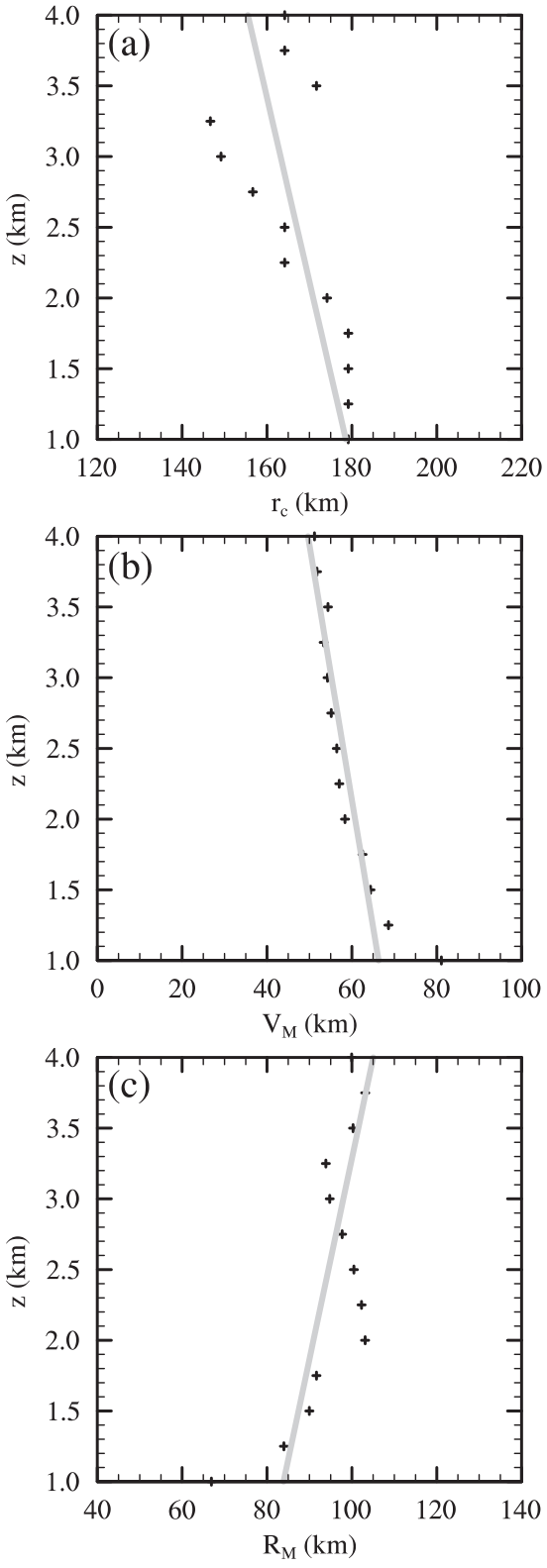

FIG. 4. (a) Input $r_c^e(z_n)$ (plotted by + signs) and estimated $r_c^a(z)$ (plotted by the gray solid line). (b) Input $V_M^e(z_n)$ and estimated $V_M^a(z)$. (c) Input $R_M^e(z_n)$ and estimated $R_M^a(z)$. All the results are produced from the same volume of v_r^{obs} as that used in Fig. 2.

linear increase fits $R_M^e(z_n)$ roughly. A qualitatively similar decrease of $V_M^a(z)$ and increase of $R_M^a(z)$ with the increase of z (from 1 to 4 km) are obtained by the refined vortex analysis from all other radar volume scans so far tested (see section 3b).

3. Adaptive dealiasing tested with velocities scanned from hurricanes and typhoons

a. Adaptive dealiasing

The new adaptive dealiasing consists of the same two main steps, the reference check and continuity check, as the AR-VAD-based dealiasing except that the abovementioned refined vortex analysis is used in place of the AR-VAD analysis to produce v_r^{ref} for the reference check in the first main step. In particular, after $\phi_+^a(z, \theta_k)$, $r_c^a(z)$, $V_M^a(z)$, and $R_M^a(z)$ are estimated by the refined vortex analysis as described in section 2, they are used as ϕ_c, r_c, V_M, and R_M, respectively, and substituted back into (3) to compute v_r^{ref} as a function of ϕ and $r(z, \theta_k)$ on each tilt over the vertical range between 1 km $\le z \le$ 4 km. The threshold condition for the alias correction in the reference check is the same as that used in X11. This threshold condition and related algorithm for the reference check are reviewed briefly below.

Preceding the reference check, all the raw data points are flagged. The reference check goes through every data point along each range circle on each tilt between 1 km $\le z \le$ 4 km. At each data point, the Nyquist folding number is estimated first by

$$N = \mathrm{Int}[(v_r^{ref} - v_r^{ref})/(2v_N)], \tag{7}$$

where Int[( )] represents the nearest integer of ( ) and v_r^{obs} is the observed raw radial velocity. If $N = 0$, then v_r^{obs} needs no correction, but the data point is deflagged with v_r^{obs} accepted as a seed datum only if

$$|v_r^{obs} - v_r^{ref}| \le v_N/4. \tag{8}$$

If $N \neq 0$, then v_r^{obs} is corrected to v_r^{cob} ($=v_r^{obs} + 2Nv_N$), but v_r^{cob} is accepted as a new seed datum (in place of the original v_r^{obs}) only if

$$|v_r^{cob} - v_r^{ref}| \le v_N/4. \tag{9}$$

If the threshold conditions (8) and (9) are both not satisfied, then the data point remains to be flagged and the check proceeds to the next data point.

The above-mentioned threshold value of $v_N/4$ implies that v_r^{ref} must be within $\pm v_N/4$ of v_r^{true} to unmistakably correct possible aliasing in v_r^{obs} and must be within $\pm 7v_N/4$ of v_r^{true} to flag (but not correct) possible alias in v_r^{obs} at each observation point. Although the original vortex

analysis in XJL can estimate V_M and R_M quite reliably and accurately, its computed v_r^{ref} may occasionally have a large error beyond $\pm 7v_N/4$, especially in the vicinity of ϕ_+. With the refinements in section 2, v_r^{ref} produced by the refined vortex analysis can have the required accuracy—that is, within $\pm v_N/4$ ($\pm 7v_N/4$) of v_r^{true}—at every observation point between 1 km $\le z \le$ 4 km on every tilt for all the 1099 volume scans of severely aliased v_r^{obs} so far tested (see the next subsection). The satisfactory performance of the refined vortex analysis makes the reference check simple and clean (without needing any additional quality check).

After the above-mentioned check, the continuity check of X11 is performed in the second main step. As described in section 2c in X11, the continuity check uses all available seed data in a properly enlarged area around each flagged data point that is being checked, so it can traverse small data gaps (up to 10 km in the radial direction or 5° in the azimuthal direction). Here, the continuity check is performed with the following modification. In the AR-VAD-based dealiasing, the reference check and its produced seed data in the first main step are limited within the cutoff radial range ($r = 30$ km for $\theta < 1°$ or $r = 80$ km for $\theta \ge 1°$) to avoid false dealiasing, and the continuity check proceeds circle by circle outward one way only from the smallest range circle (covered by the seed data) to the largest range circle on each tilt. In the new adaptive dealiasing, however, the reference check and its produced seed data cover a wide radial range (over the depth between 1 km $\le z \le$ 4 km) on each tilt, so the continuity check can easily start from the smallest range circle covered by the seed data and go outward to the largest range circle first and then come back inward to the smallest range circle (below $z =$ 1 km) and thus complete the entire tilt.

b. Test results with hurricanes

The new adaptive dealiasing described in the previous subsection has been successfully tested with 602 volumes of severely aliased v_r^{obs} scanned from three hurricane cases by four operational WSR-88D radars [KLIX (Slidell, Louisiana), KMOB (Mobile, Alabama), KHGX (Houston, Texas), KMHX (Morehead City, North Carolina)]. Among the 602 volume scans, 52 volumes were scanned by the KLIX radar from Hurricane Katrina over the entire period from 0900 to 1400 UTC 29 August 2005; 110 volumes were scanned by the KMOB radar from Hurricane Katrina from KMOB radar over the entire period from 1200 to 2200 UTC 29th August 2005; 235 volumes were scanned by the KHGX radar from Hurricane Ike over the entire period from 0900 to 1900 UTC 13 September 2008; and 205 volumes were scanned by the KMHX radar from Hurricane Irene over the entire period from 0500 to 2100 UTC 27 August 2011. An example is given in Fig. 5.

Figure 5a shows the image of raw v_r^{obs} at the lowest tilt ($\theta_1 = 0.5°$) scanned by the operational KLIX radar at 1028 UTC 29 August 2005 from Hurricane Katrina. This lowest tilt is from the same volume of v_r^{obs} as that used to produce Fig. 2, the spatial resolutions are 250 m in the radial direction and 1° in the azimuthal direction, and the maximum detection range of the radar is 175 km in this case. At this time, the hurricane vortex center (marked by the yellow C in Fig. 5a) was about 160 km to the south (with $\phi_c \approx 175°$) of the KLIX radar. Since the Nyquist velocity ($v_N = 21.5$ m s^{-1}) used by this scan is much smaller than the estimated $V_M{}^a(z)$ (= 66.3 m s^{-1} at $z = 1$ km) and therefore must be much smaller than the absolute values of the true maximum positive and negative radial velocities, the observed radial velocities are severely aliased in two main areas (marked by the two white A letters) on the two sides of the southern zero-v_r line [estimated by $\phi_+{}^a(z, \theta_1)$ with z viewed as a function of r] on $\theta_1 = 0.5°$. The small red area inside the large green area to the southeast of the radar site shows doubly aliased raw v_r^{obs}.

Figure 5b shows that v_r^{ref} produced by the refined vortex analysis (between 1 km $\le z \le$ 4 km—that is, 75 km $\le r \le$ 198 km—but plotted only over the v_r^{obs}-covered area) can capture the gross structure and magnitude of v_r^{true}, including the southern zero-v_r line and the positive and negative maxima of v_r^{true} on its two sides. Figure 5c shows that the seed data produced by the reference check are free of false dealiasing and cover sufficiently broad areas, so the subsequent continuity check can correct most aliases with no false dealiasing, as shown in Fig. 5d. As listed in the first row of Table 1, the rejected data are only 0.17% of the total raw data, so the accepted alias-free data are 99.83% of the total on this lowest tilt. The AR-VAD-based dealiasing (X11) is also alias free as shown in Fig. 5e but its rejected data are 14.76% of the total on this tilt, so it underperforms the new adaptive dealiasing (not only on this lowest tilt but also over the entire volume, as shown in Table 1). The extended AR-Var-based dealiasing (X13) is alias free and its rejected data are 1.04% of the total on this tilt, so it only slightly underperforms the new adaptive dealiasing on the lowest tilt (as well as for the entire volume, as shown in Table 1) but the computational time is increased by nearly 4 times (from 15 to 56 s of CPU time for dealiasing the entire volume on a Dell XII computer). The operationally used dealiasing (Eilts and Smith 1990) rejects no datum but it is not alias-free, as shown in Fig. 5f (also see the last column in Table 1).

As the vortex center of Hurricane Katrina moved northward into the 100-km radial range of the KLIX radar in the later time period (1332–1338 UTC 29 August

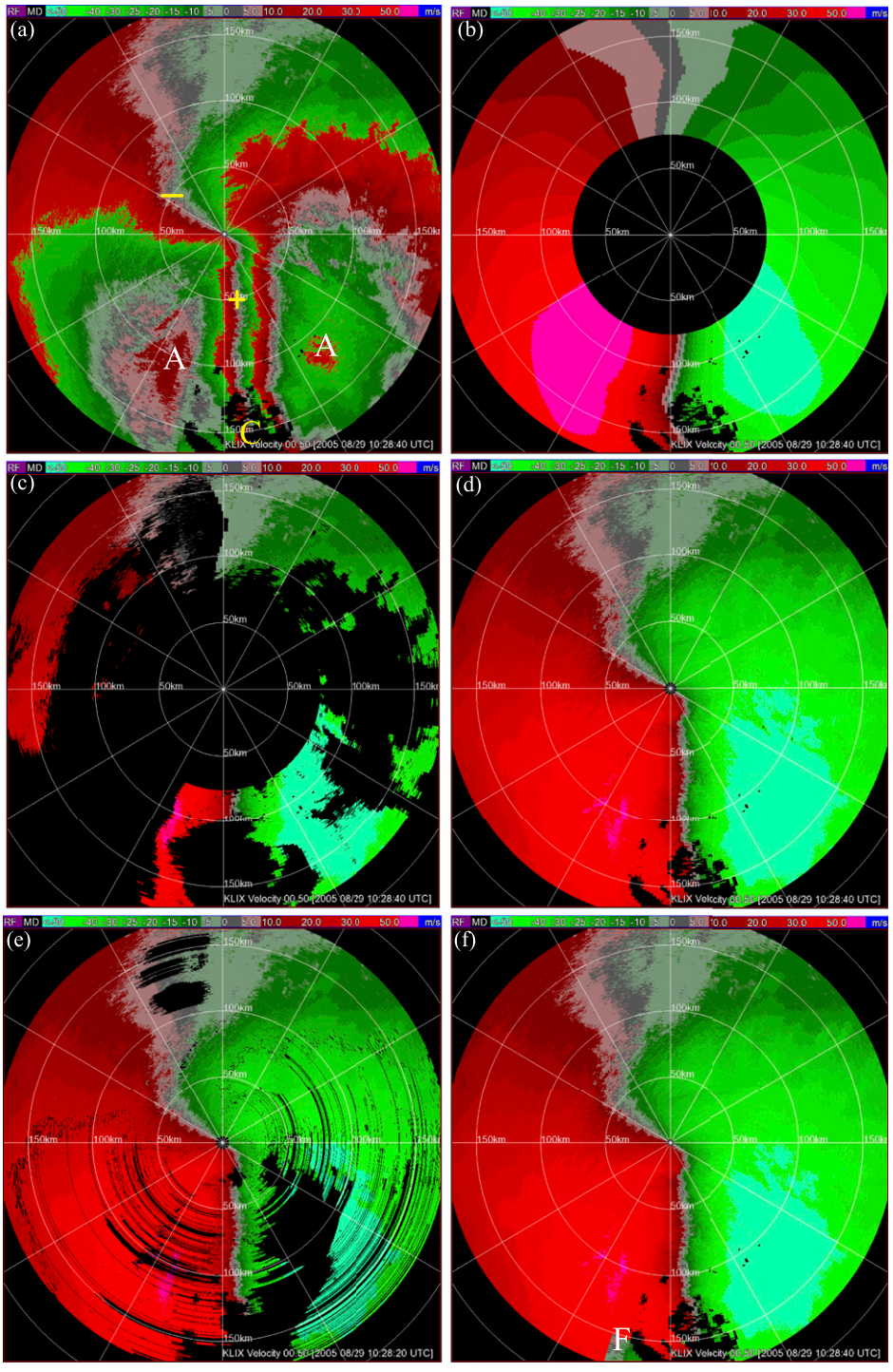

FIG. 5. (a) Image of raw v_r^{obs} on the lowest tilt ($\theta_1 = 0.5°$) scanned with $v_N = 21.5\ \text{m s}^{-1}$ from Hurricane Katrina by the KLIX radar at 1028 UTC 29 Aug 2005. (b) Image of v_r^{ref} produced by the refined vortex analysis. (c) Image of seed data produced by the reference check. (d) Image of dealiased v_r^{obs} produced by the new adaptive dealiasing. (e) Image of dealiased v_r^{obs} produced by the VAD-based dealiasing (X11). (f) Image of dealiased v_r^{obs} produced by the operationally used method (Eilts and Smith 1990). The lowest tilt of raw v_r^{obs} in (a) is from the same volume of v_r^{obs} as that used in Fig. 2. In (a), the yellow + and − signs mark the two zero-v_r points ϕ_+ and ϕ_-, respectively, on the range circle of $r \approx 50$ km; the yellow C marks the hurricane vortex center, which is at $(r, \phi) = (r_c, \phi_c) \approx (160\,\text{km}, 175°)$ in the radar coordinates; and the two white A's mark the two severely aliased areas. In (f), the white letter F marks false dealiasing in the small green area. The color scale on the top of each panel shows red (green) for positive (negative) value, that is, $v_r > 0$ ($v_r < 0$) for an outward (inward) radial component velocity.

TABLE 1. Performances of the new adaptive method vs the AR-VAD-based method (×11), the extended AR-Var-based method (×13), and the operational method (Eilts and Smith 1990) for the 14 tilts of the entire volume scanned by the operational KLIX radar at 1028 UTC 29 Aug 2005 from Hurricane Katrina (see Fig. 5). The percentage of incorrectly accepted aliased data (rejected data) from the raw data is listed for each tilt in each row and for the entire volume in the last row along the left (right) column under each method. Data within $r < 5$ km for $\theta < 3°$ and within $r < 2.5$ km for $\theta \geq 3°$ are likely contaminated and thus excluded from the raw data.

		New adaptive method		AR-VAD-based method		AR-VAR-based method		Operational method	
Tilt	No. of raw data	Aliased data (%)	Rejected data (%)	Aliased data (%)	Rejected data (%)	Aliased data (%)	Rejected data (%)	Aliased data (%)	Rejected data (%)
$\theta_1 = 0.5°$	240 654	0	0.17	0	14.76	0	1.04	0.30	0
$\theta_2 = 1.45°$	238 334	0	0.25	0	16.35	0	0.43	41.41	0
$\theta_3 = 2.4°$	234 502	0	0.30	0	12.99	0	0.30	97.54	0
$\theta_4 = 3.35°$	210 582	0	0.23	0	9.05	0	0.36	94.34	0
$\theta_5 = 4.3°$	179 334	0	0.23	0	8.04	0	0.78	66.26	0
$\theta_6 = 5.25°$	152 699	0	0.45	0	14.28	0	0.59	0.22	0
$\theta_7 = 6.2°$	133 924	0	0.86	0	9.83	0	0.87	0.05	0
$\theta_8 = 7.5°$	118 373	0	1.82	0	4.41	0	1.89	0.07	0
$\theta_9 = 8.7°$	105 520	0	0.58	0	0.80	0	0.61	81.26	0
$\theta_{10} = 10°$	94 157	0	0.36	0	1.55	0	0.30	0	0
$\theta_{11} = 12°$	81 745	0	0.41	0	1.15	0	0.15	0	0
$\theta_{12} = 14°$	71 143	0	1.22	0	6.76	0	0.39	0	0
$\theta_{13} = 16.7°$	60 436	0	0.67	0	50.83	0	0.20	0	0
$\theta_{14} = 19.5°$	51 833	0	1.68	0	57.94	0	0.17	0	0
All 14 tilts	1 973 236	0	0.51	0	12.54	0	0.62	36.88	0

2005), the aliased raw v_r^{obs} scanned by the KLIX radar became increasingly difficult to correct for the three previously developed dealiasing methods but not for the new adaptive dealiasing. For the aliased raw v_r^{obs} scanned in this later time period, the operationally used dealiasing often produces falsely dealiased data over large areas, while the AR-VAD-based dealiasing and the extended AR-Var-based dealiasing occasionally fail to produce v_r^{ref} and thus no seed and no alias correction, especially in the hurricane core area covered by the radar scans (where the increased complexity of the true winds invalidates the uniform-wind approximation required by the AR-VAD analysis and by the first guess in the AR-Var analysis). Similar results and comparisons are seen for the aforementioned 602 volumes scanned by the WSR-88D radars from hurricanes in the United States.

c. *Test results for typhoons*

The method is also tested with 497 volumes of severely aliased v_r^{obs} scanned from six typhoon cases by operational CINRAD/SA radars in China, and the method is found to be almost free of false dealiasing except for one tilt (at $\theta_1 = 0.6°$) scanned by the operational Yangjiang, China (Z9662), radar at 1936 UTC 23 September 2008 from Typhoon Hagupit. As shown by the image of raw v_r^{obs} on this tilt ($\theta_1 = 0.6°$) in Fig. 6a, the typhoon vortex center (marked by the yellow C in Fig. 6a) was about 68 km to the south (with $\phi_c \approx 182°$) of the Yangjiang radar at this time. The Nyquist velocity v_N (=26.8 m s^{-1}) used on this tilt is significantly smaller than the estimated $V_M^a(z)$ (= 59.5 m s^{-1} at $z = 1$ km), so the raw radial velocities are severely aliased in two main areas (marked by the two white A's) on the two sides of the southern zero-v_r line [estimated by $\phi_+^a(z, \theta_1)$ with z viewed as a function of r] on $\theta_1 = 0.6°$. By extrapolating $r_c^a(z)$, $V_M^a(z)$, and $R_M^a(z)$ to $z < 1$ km but with $\phi_+^a(z, \theta_1)$ estimated in L_1 for $z < 1$ km according to step 3 in section 2c, the v_r^{ref} field is produced on this lowest tilt by the refined vortex analysis with the radial range of 68 km $\leq r \leq$ 186 km (associated with the vertical range of 1 km $\leq z \leq$ 4 km on $\theta_1 = 0.6°$) extended inward from $r = 68$ km to $r = 5$ km (i.e., downward below $z = 1$ km) for the reason explained later. As shown in Fig. 6b, this v_r^{ref} field can roughly capture the structure and magnitude of v_r^{true}, including the southern zero-v_r line and the positive and negative maxima of v_r^{true} on its two sides.

Figure 6c shows that the seed data produced by the reference check are free of alias and cover sufficiently broad areas, although the coved areas are sparse to the north and northeast of the radar. Figure 6d shows that the continuity check using the seed data between 68 km $\leq r \leq$ 186 km (associated with the vertical range of 1 km $\leq z \leq$ 4 km on $\theta_1 = 0.6°$) in Fig. 6c can correct aliases over most data areas except for the small sector area (marked by the white F) between $150° < \phi < 190°$ within $r < 55$ km. This small sector area contains the zero-v_r line (as shown in Fig. 6a), so the true radial velocities are small and the raw data are not aliased in this small sector area. However, as shown in Fig. 6a, the raw data are very noisy not only in this small sector area but also in the adjacent sector area of aliased raw data between

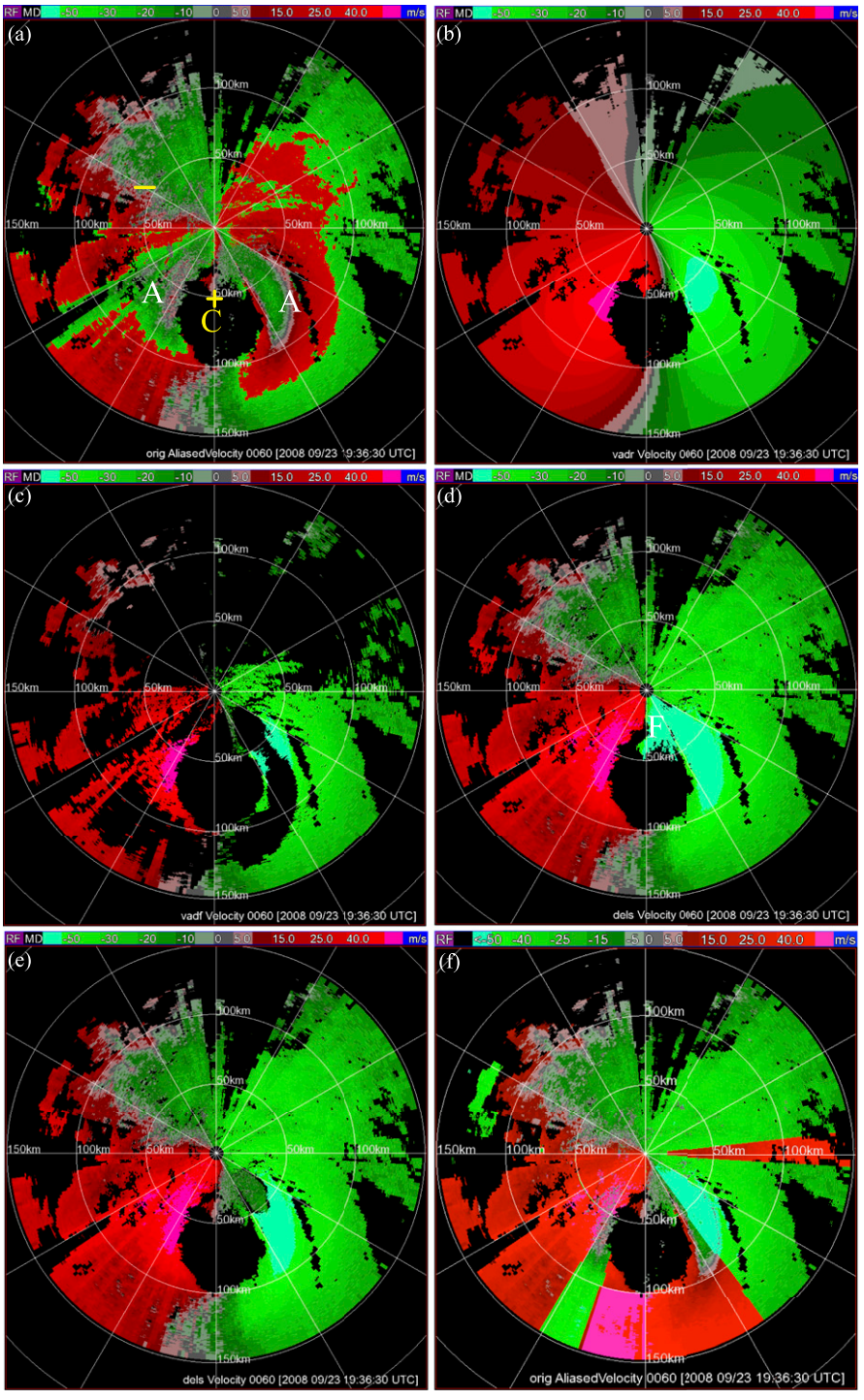

FIG. 6. The first four and last panels are as in Figs. 5a–d and 5f, respectively, but for the lowest tilt ($\theta_1 = 0.6°$) scanned with $v_N = 26.8\,\mathrm{m\,s^{-1}}$ from Typhoon Hagupit by the operational Yangjiang (Z9662) radar at 1135 UTC 23 Sep 2008. The v_r^{ref} field in (b) and the seed data in (c) are no longer confined in the radial range of 68 km $\le r \le$ 186 km (associated with the vertical range of 1 km $\le z \le$ 4 km on $\theta_1 = 0.6°$) but extended inward from $r = 68$ km to $r = 5$ km (i.e., downward below $z = 1$ km on $\theta_1 = 0.6°$). (e) The image of the finally dealiased data produced by the continuity check using all the seed data in (c), that is, not only those confined between 68 km $\le r \le$ 186 km but also the additional seed data within $r < 68$ km. In (f) the image of dealiased v_r^{obs} produced by operationally used dealiasing (Eilts and Smith 1990) is shown. The typhoon vortex center, marked by the yellow C in (a), is at $(r, \phi) = (r_c, \phi_c) \approx (68\,\mathrm{km}, 182°)$ in the radar coordinates. The white F in (d) marks the small sector area of false dealiasing between $150° < \phi < 190°$ within $r < 55$ km.

TABLE 2. As in Table 1, but for the nine tilts of the entire volume scanned by the operational Yangjiang (Z9662) radar at 1936 UTC 23 Sep 2008 from Typhoon Hagupit (see Figs. 6 and 7). The right column under the operational method is omitted because no datum (0%) is rejected. The reduced percentage, 1.69% (0.26%), listed in the parentheses in the first (last) row in the right column under the new adaptive method shows the improved result by using the extended reference check (see Fig. 6e).

		New adaptive method		AR-VAD-based method		Extended AR-VAR-based method		Operational method
Tilt	No. of raw data	Aliased data (%)	Rejected data (%)	Aliased data (%)	Rejected data (%)	Aliased data (%)	Rejected data (%)	Aliased data (%)
$\theta_1 = 0.6°$	158 266	3.57 (1.69)	2.86	10.29	34.20	0	100	16.36
$\theta_2 = 1.6°$	181 291	0	0.76	0	33.40	0	0.99	6.34
$\theta_3 = 2.5°$	173 843	0	0.18	0	30.87	0	0.28	62.55
$\theta_4 = 3.5°$	155 400	0	0.20	0	36.19	0	0.66	60.68
$\theta_5 = 4.4°$	128 091	0	0.43	0	42.24	0	1.25	62.48
$\theta_6 = 6.5°$	90 263	0	0.94	0	47.78	0	7.98	1.43
$\theta_7 = 10$	61 654	0	0.80	0	62.05	0	100	64.49
$\theta_8 = 14.7°$	48 620	0	0.87	0	100	0	100	97.81
$\theta_9 = 19.6°$	40 367	0	6.19	0	100	0	100	98.34
All 9 tilts	1 037 795	0.54 (0.26)	1.09	1.57	43.27	0	30.93	43.29

$120° < \phi < 152°$ within 10 km $< r <$ 125 km. These two sector areas of very noisy data are connected (around the radial of $\phi = 150°$) quite homogeneously, which makes it very difficult to exactly identify the boundary between the two (nonaliased and aliased) areas even with human expertise. Thus, as the continuity check goes radially inward (from the seed data points in Fig. 6c), the aliased raw data in the above-mentioned second sector area (between $120° < \phi < 152°$ within 10 km $< r <$ 125 km) are correctly dealiased first, and then the nonaliased raw data in the above-mentioned first sector area (between $150° < \phi < 190°$ within $r <$ 55 km) are falsely dealiased due to the very noisy and homogeneous connection between the two sector areas. There are 5653 falsely dealiased data on the lowest tilt only, so the percentage of incorrectly accepted aliased data is 3.57% on this tilt (merely 0.54% for the entire volume) as listed in the first (last) row of Table 2. Such a failure of the continuity check (or any other type of continuity check) is clearly inevitable in this very difficult case, and the difficulty is caused by high data noise and poor data quality in this rarely encountered case.

When the v_r^{ref} field in Fig. 6b is used not only between 68 km $\le r \le$ 186 km but also within $r <$ 68 km, the reference check can produce additional seed data in the aforementioned two sectors of very noisy data as revealed in Fig. 6c. These additional seed data can reduce falsely dealiased data produced by the continuity check in the second main step. With this approach, the dealiased data produced by the continuity check are shown in Fig. 6e, where the number of falsely dealiased data is reduced from 5653 to 2670 and thus the percentage of incorrectly accepted aliased data is reduced from 3.57% to 1.69% on the lowest tilt (from 0.54% to 0.26% for the entire volume) as listed in the first (last) row of Table 2. This extended reference check can improve dealiasing in the above-mentioned rarely encountered difficult case, but it also increases the risk of producing falsely dealiased seed data in the first main step. For all other tilts and volumes so far tested, such an extension is risky and unnecessary. For this very difficult case, the AR-VAD-based dealiasing is not free of alias, its incorrectly accepted aliased data are 10.29% , and its rejected data are 34.20% of the total, as listed in the first row of Table 2. The extended AR-Var-based dealiasing rejects all the data and thus fails to work on this tilt (see the first row of Table 2). The operationally used dealiasing rejects no datum, but its accepted data are severely aliased, as shown in Fig. 6f. Its incorrectly accepted aliased data are 16.36% (43.29%) of the total on the lowest tilt (over the entire volume) as listed in last column of Table 2.

The above-mentioned difficulty is seen at the lowest tilt ($\theta_1 = 0.6°$) of merely one volume scan. For other higher tilts in this volume and any tilts (including the lowest tilts) of the other 496 volumes (scanned by operational CINRAD/SA radars in China) so far tested, the method is free of false dealiasing. As an example, Fig. 7a shows the image of raw v_r^{obs} on the second lowest tilt (at $\theta_2 = 1.6°$) for the same volume as in Fig. 6. Again, the Nyquist velocity v_N (= 26.8 m s^{-1}) used on this tilt is significantly smaller than the estimated $V_M^a(z)$ (=59.5 m s^{-1} at $z = 1$ km), so the observed radial velocities are severely aliased in two main areas (marked by the two white A's) on the two sides of the southern zero-v_r line [estimated by $\phi_+^a(z, \theta_2)$ with z viewed as a function of r] on $\theta_2 = 1.6°$. Figure 7b shows that v_r^{ref} produced by the refined vortex analysis (between 1 km $\le z \le$ 4 km—that is, 34.3 km $\le r \le$ 116.8 km—but plotted only over the v_r^{obs}-covered area) can capture the gross structure and magnitude of v_r^{true}, including the southern zero-v_r line and the positive and

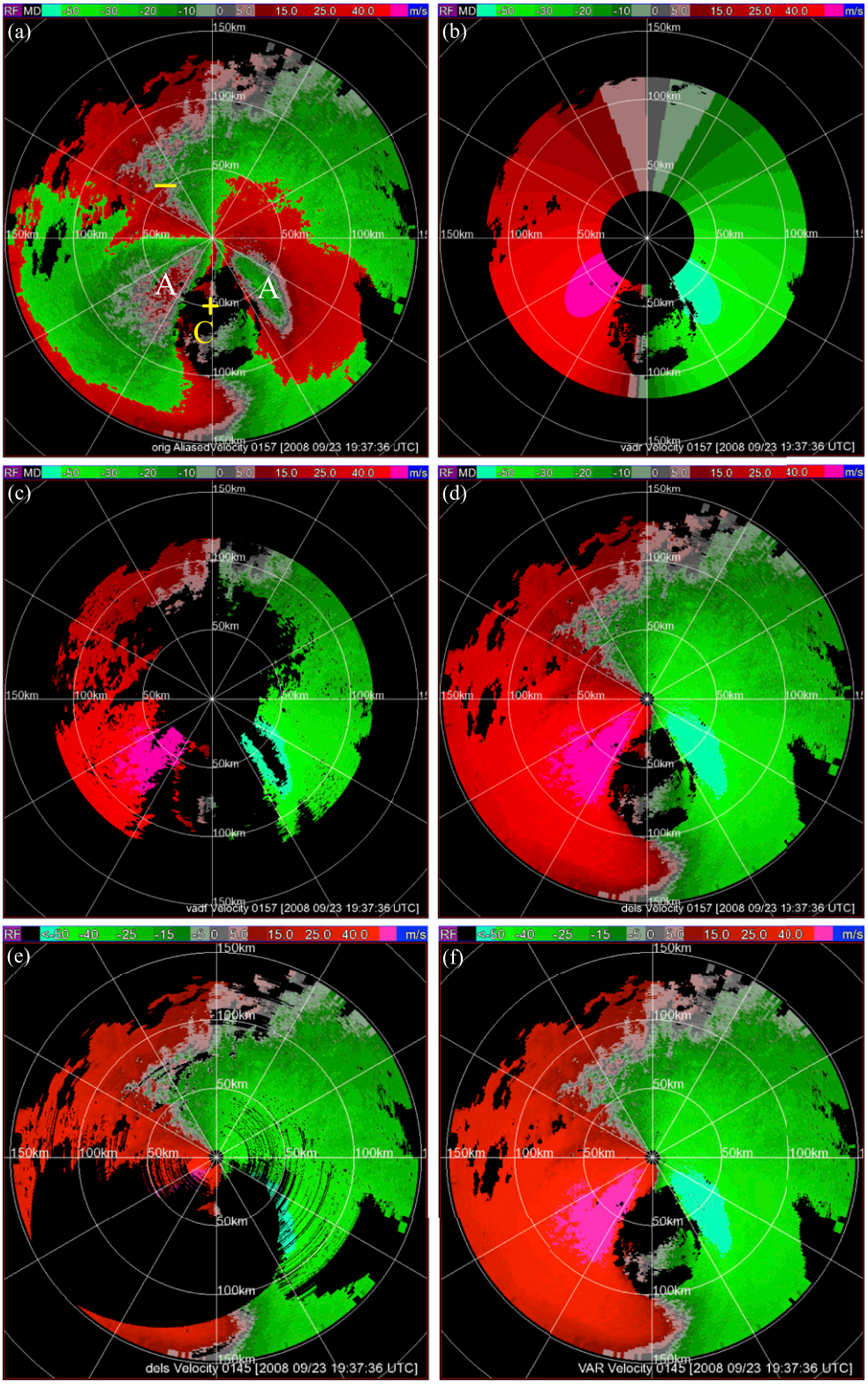

FIG. 7. The first five panels are as in Figs. 5a–e, but for the second lowest tilt at $\theta_2 = 1.6°$ in the same volume scanned from Typhoon Hagupit by the operational Yangjiang (Z9662) radar as that in Fig. 6. (f) The image of dealiased v_r^{obs} produced by the extended AR-Var-based dealiasing (X13).

negative maxima of v_r^{true} on its two sides. Figure 7c shows that the seed data produced by the reference check are free of false dealiasing and cover sufficiently broad areas, so the subsequent continuity check can correct most aliases with no false dealiasing as shown in Fig. 7d and the rejected data are only 0.76% of the total on this tilt as listed in the second row of Table 2.

The AR-VAD-based dealiasing is alias free on the second lowest tilt as shown in Fig. 7e, but its rejected data are 33.40% (43.27%) of the total on this tilt (over the entire volume), as shown in Table 2. The extended AR-Var-based dealiasing is alias free on the second lowest tilt as shown in Fig. 7f, while its rejected data are 0.99% (30.93%) of the total on this tilt (over the entire volume) and this percentage is lower than that rejected by the AR-VAD-based dealiasing but higher than that rejected by the new adaptive dealiasing, as shown in Table 2.

The new adaptive dealiasing also works well with no false dealiasing for all 60 volumes of severely aliased v_r^{obs} scanned from this typhoon (Typhoon Hagupit) during the time period of 0700–1400 UTC 23 September 2008 and the 437 volumes from five other typhoons. These 437 volumes include 60 volumes from Typhoon Metsa scanned by the operational Ningbo, China (Z9574), radar during the time period of 0400–1200 UTC 5 August 2005, 10 volumes from Typhoon Chanthu scanned by the operational Zhanjiang, China (Z9759), radar during the time period of 1200–1400 UTC 22 July 2010, 81 volumes from Typhoon Utor by the operational Yangjiang (Z9662) radar during the time period of 0000–0800 UTC 14 August 2013, 105 volumes from Typhoon Usagi scanned by the operational Shanwei, China (Z9660), radar during the time period of 0000–1025 UTC 22 September 2013, and 181 volumes from Typhoon Fitow scanned by the operational Wenzhou, China (Z9577), radar during the time period of 0130–2000 UTC 6 October 2013. For the 1099 volume scans so far tested, the new adaptive dealiasing never fails to work even when the raw data coverage becomes poor (close to or slightly less than 180° on most range circles).

4. Conclusions

The techniques presented in this paper refine the vortex analysis of XJL so it can be used in place of the AR-VAD analysis (X10) to improve the reference check in dealiasing. This upgrades the VAD-based dealiasing (X11) to a new adaptive dealiasing method applicable solely to raw radial velocities scanned from hurricanes and typhoons. This new adaptive method has been tested successfully with 602 volumes of severely aliased radial velocities scanned from hurricanes in the United States. The method has been also successfully tested with 497 volumes of severely aliased v_r^{obs} scanned from six typhoon cases by operational CINRAD/SA radars in China. The dealiasing results were verified with human expertise by carefully viewing the enlarged radial velocity images pixel by pixel on each tilt for all the tilts in the 1099 volumes. According to these verifications, the new adaptive dealiasing outperforms the operationally used dealiasing (Eilts and Smith 1990) in all the cases so far tested, and it works very well as long as the vortex center is within the 200-km radial range from the radar. It can correct most aliases on each tilt with no false dealiasing (except for a small sector area on one tilt where the raw data are very noisy with poor quality as examined in Fig. 6), so it cannot only satisfy the high-quality standard required by data assimilating but also reject less or much less data than the extended AR-Var-based dealiasing (X13) and the AR-VAD-based dealiasing for hurricanes and typhoons, especially when the hurricane or typhoon is close to the radar (within 100-km radial range). The new adaptive dealiasing is more efficient (by nearly 4 times) than the extended AR-Var-based dealiasing and satisfies the computer time constraint explained in the introduction, and it can be used safely as long as the hurricane or typhoon center is within the 200-km radial range.

In this paper, the AR vortex analysis is refined and used for the reference check in the second main step of dealiasing, but the analysis is confined between $1\,\text{km} \le z \le 4\,\text{km}$ (except for one rare case in which the analysis is extended below 1 km on the lowest tilt, as shown in Fig. 6b) for the following two reasons. First, the analysis tends to become unreliable in the middle troposphere and beyond ($z > 4\,\text{km}$), where the environmental mean wind is often significant but not considered in the vortex model [see (1) and (2)]. Second, the analysis also tends to become unreliable or even completely inapplicable in the boundary layer, where the radial wind becomes strong toward the hurricane eyewall [as implied by the rapid change of the estimated ϕ_+ with z ($\le$1 km) in each panel of Fig. 2] but not considered in the vortex model. With the first limitation, the reference radial velocity field and subsequent continuity check on a middle tilt ($3° < \theta < 5°$) cannot cover isolated raw data patches (if any), so these patches will remain to be flagged and thus finally rejected. It is possible to extend the analysis beyond $z = 4\,\text{km}$, and this may improve the dealiased data coverage on middle tilts. Such an extension deserves further investigations.

Multiple pulse repetition frequency (PRF) scans have been used occasionally and optionally (with VCP121 and VCP221) by NOAA operational WSR-88D radars for hurricanes. A multi-PRF dealiasing algorithm has been developed and applied to multi-PRF scans to improve the reliability of dealiasing, but regions with only velocity data from the scan using PRF with the largest

unambiguous range still can have dealiasing errors, as the Nyquist velocity is reduced to $v_N \approx 20\,\mathrm{m\,s^{-1}}$ (Zittel et al. 2008). By setting v_N differently according to different PRF for the cost function in (6) of this paper, the new adaptive dealiasing presented in this paper can be extended to improve the multi-PRF dealiasing algorithm for hurricanes. Such an extension deserves continued research beyond this paper.

Acknowledgments. We are thankful to Kang Nai of the University of Oklahoma (OU) for providing the continuity check subroutines and plotting for Figs. 5–7, and to the anonymous reviewers for their comments and suggestions, which improved the presentation of the paper. The research was supported by the ONR Grant N000141410281 to OU. Funding was also provided by China Meteorological Administration Special Public Welfare Research Fund (GYHY201506004 and GYHY201506021), the National Natural Sciences Foundation of China (Grant 91337103), the National Key Technology R&D Program (2012BAC22B02), and National Program on Key Basic Research Project (973 Program, 2013CB430106) of China.

APPENDIX

Glossary of Variables and Symbols

a_j	Coefficient for the constant part of the fitting function in the jth layer
b_j	Coefficient for the linear part of the fitting function in the jth layer (see section 2c)
J	Cost function defined by (6) in the space of (V_M, R_M)
$J^{\min}(r_c)$	Global minimum of J for given r_c
L_j	jth vertical layer
N	Nyquist number
R	Radial distance from vortex center
R_M	R where V_T reaches V_M
$R_M{}^{\min}(r_c)$	R_M at the global minimum point of J for given r_c
$R_M{}^e(z_n)$	$R_M{}^{\min}(r_c)$ for $r_c = r_c{}^e$ at nth vertical level
$R_M{}^a(z)$	Linear function of z estimated for R_M from $R_M{}^e(z_n)$ (see section 2d)
V_M	Maximum value of V_T
$V_M{}^{\min}(r_c)$	V_M at the global minimum point of J for given r_c
$V_M{}^e(z_n)$	$V_M{}^{\min}(r_c)$ for $r_c = r_c{}^e$ at nth vertical level
$V_M{}^a(z)$	Linear function of z estimated for V_M from $V_M{}^e(z_n)$ (see section 2d)
V_T	Tangential velocity of modeled vortex in (1)
Δh	Depth (=1 km) of each vertical layer
r	Radial distance from radar
r_c	Radial distance of vortex center from radar
$r_c{}^e$	Refined estimate of r_c (at a selected vertical level
$r_c{}^a(z)$	Linear function of z estimated for r_c from $r_c{}^e(z_n)$ (see section 2d)
v_N	Nyquist velocity
v_r	Radial velocity–velocity component along the radar beam (positive for outward)
$v_r{}^{\mathrm{mod}}$	Modeled v_r in (2) and (3)
$v_r{}^{\mathrm{obs}}$	Observed v_r by radar
$v_r{}^{\mathrm{ref}}$	Reference v_r produced by the AR vortex analysis in section 3a
$v_r{}^{\mathrm{true}}$	True v_r
z	Height above radar
z_0	Lowest vertical level (at z = 250 m) in dealiasing
z_n	Height of nth vertical level
Δz	Vertical interval (=25 m)
α	Azimuthal angle of measurement point viewed from vortex center
ϕ	Azimuthal angle of measurement point viewed from radar
ϕ_+	Zero-v_r point with $\partial_\phi v_r > 0$ on a range circle
ϕ_-	Zero-v_r point with $\partial_\phi v_r < 0$ on a range circle
ϕ_c	Azimuthal angle of vortex center viewed from radar
$\phi_c{}^{\mathrm{op}}$	Preestimated ϕ_c from operationally issued hurricane location information
$\phi^{\mathrm{obs}}{}_0$	Observation point where $\lvert v_r{}^{\mathrm{obs}}\rvert$ reaches a local minimum below 2 m s^{-1} on a range circle
$\phi^{\mathrm{obs}}{}_+$	ϕ_0^{obs} point (if exists) in the immediate vicinity of the true ϕ_+ on a range circle
$\phi_+(z_n)$	ϕ_+ constructed as single discrete function of z_n from $\phi_+(z_n, \theta_k)$ (see Fig. 2b)
$\phi_+{}^a(z)$	Continuous function of z estimated for ϕ_+ from $\phi_+(z_n)$ (see Fig. 2b)
$\phi_+{}^a(z_n, \theta_k)$	Estimated ϕ_+ at nth vertical level on kth tilt (see Fig. 2a)
$\phi_+{}^a(z, \theta_k)$	Continuous function of z estimated for ϕ_+ from $\phi_+{}^a(z_n, \theta_k)$ on kth tilt (see Fig. 2c)
$\Delta\phi$	Maximum half-window width (=15°) for searching ϕ_+ around each ϕ_0^{obs}
$\Delta\phi_L$	Left half-window width for searching ϕ_+ around each ϕ_0^{obs}
$\Delta\phi_R$	Right half-window width for searching ϕ_+ around each ϕ_0^{obs}
$\Delta\phi_j$	Half-window width for filtering data points in jth layer (see Figs. 2a and 2b)

θ'	Slope angle of radar beam relative to Earth's surface beneath measurement point
θ	Elevation angle of radar beam at the radar site
θ_k	θ for kth tilt
θ_K	θ for the highest tilt (with $k = K$)
$\partial_\phi v_r$	Azimuthal derivative of v_r

REFERENCES

Browning, K. A., and R. Wexler, 1968: The determination of kinematic properties of a wind field using Doppler radar. *J. Appl. Meteor.*, **7**, 105–113, doi:10.1175/1520-0450(1968)007<0105:TDOKPO>2.0.CO;2.

Doviak, R. J., and D. S. Zrnić, 2006: *Doppler Radar and Weather Observations*. 2nd ed. Dover Publications, 562 pp.

Eilts, M. D., and S. D. Smith, 1990: Efficient dealiasing of Doppler velocities using local environment constraints. *J. Atmos. Oceanic Technol.*, **7**, 118–128, doi:10.1175/1520-0426(1990)007<0118:EDODVU>2.0.CO;2.

Gao, J., K. K. Droegemeier, J. Gong, and Q. Xu, 2004: A method for retrieving mean horizontal wind profiles from single-Doppler radar observations contaminated by aliasing. *Mon. Wea. Rev.*, **132**, 1399–1409, doi:10.1175/1520-0493(2004)132<1399:AMFRMH>2.0.CO;2.

Gong, J., L. Wang, and Q. Xu, 2003: A three-step dealiasing method for Doppler velocity data quality control. *J. Atmos. Oceanic Technol.*, **20**, 1738–1748, doi:10.1175/1520-0426(2003)020<1738:ATDMFD>2.0.CO;2.

Haase, G., and T. Landelius, 2004: Dealiasing of Doppler radar velocities using a torus mapping. *J. Atmos. Oceanic Technol.*, **21**, 1566–1573, doi:10.1175/1520-0426(2004)021<1566:DODRVU>2.0.CO;2.

Harasti, P. R., C. J. McAdie, P. P. Dodge, W.-C. Lee, J. Tuttle, S. T. Murillo, and F. D. Marks, 2004: Real-time implementation of single-Doppler radar analysis methods for tropical cyclones: Algorithm improvements and use with WSR-88D display data. *Wea. Forecasting*, **19**, 219–239, doi:10.1175/1520-0434(2004)019<0219:RIOSRA>2.0.CO;2.

Jing, Z., and G. Wiener, 1993: Two-dimensional dealiasing of Doppler velocities. *J. Atmos. Oceanic Technol.*, **10**, 798–808, doi:10.1175/1520-0426(1993)010<0798:TDDODV>2.0.CO;2.

Liu, S., and Coauthors, 2009: WSR-88D radar data processing at NCEP. *34th Conf. on Radar Meteorology*, Williamsburg, VA, Amer. Meteor. Soc., 14.2. [Available online at https://ams.confex.com/ams/34Radar/techprogram/paper_156011.htm.]

Murillo, S. T., W.-C. Lee, M. M. Bell, G. M. Barnes, F. D. Marks, and P. P. Dodge, 2011: Intercomparison of ground-based velocity track display (GBVTD)-retrieved circulation centers and structures of Hurricane Danny (1997) from two coastal WSR-88Ds. *Mon. Wea. Rev.*, **139**, 153–174, doi:10.1175/2010MWR3036.1.

Tabary, P., G. Scialom, and U. Germann, 2001: Real-time retrieval of the wind from aliased velocities measured by Doppler radars. *J. Atmos. Oceanic Technol.*, **18**, 875–882, doi:10.1175/1520-0426(2001)018<0875:RTROTW>2.0.CO;2.

Vatistas, G. H., V. Kozel, and W. C. Mih, 1991: A simpler model for concentrated vortices. *Exp. Fluids*, **11**, 73–76, doi:10.1007/BF00198434.

Witt, A., R. A. Brown, and Z. Jing, 2009: Performance of a new velocity dealiasing algorithm for the WSR-88D. *34rd Conf. on Radar Meteorology*, Williamsburg, VA, Amer. Meteor. Soc., P4.8. [Available online at https://ams.confex.com/ams/34Radar/techprogram/paper_155951.htm.]

Xu, Q., 2009: Bayesian perspective of the unconventional approach for assimilating aliased radar radial velocities. *Tellus*, **61A**, 631–634, doi:10.1111/j.1600-0870.2009.00413.x.

——, and K. Nai, 2012: An adaptive dealiasing method based on variational analysis for radar radial velocities scanned with small Nyquist velocities. *J. Atmos. Oceanic Technol.*, **29**, 1723–1729, doi:10.1175/JTECH-D-12-00145.1.

——, and ——, 2013: A two-step variational method for analyzing severely aliased radar velocity observations with small Nyquist velocities. *Quart. J. Roy. Meteor. Soc.*, **139**, 1904–1911, doi:10.1002/qj.2075.

——, ——, and L. Wei, 2010: Fitting VAD wind to aliased radial-velocity observations: A minimization problem with multiple minima. *Quart. J. Roy. Meteor. Soc.*, **136**, 451–461, doi:10.1002/qj.589.

——, ——, ——, P. Zhang, S. Liu, and D. Parrish, 2011: A VAD-based dealiasing method for radar velocity data quality control. *J. Atmos. Oceanic Technol.*, **28**, 50–62, doi:10.1175/2010JTECHA1444.1.

——, ——, S. Liu, C. Karstens, T. Smith, and Q. Zhao, 2013: Improved Doppler velocity dealiasing for radar data assimilation and storm-scale vortex detection. *Adv. Meteor.*, **2013**, 562386, doi:10.1155/2013/562386.

——, Y. Jiang, and L. Liu, 2014: Fitting parametric vortices to Doppler velocities scanned from hurricanes. *Mon. Wea. Rev.*, **142**, 94–106, doi:10.1175/MWR-D-12-00362.1.

Yamada, Y., and M. Chong, 1999: VAD-based determination of the Nyquist interval number of Doppler velocity aliasing without wind information. *J. Meteor. Soc. Japan*, **77**, 447–457.

Zhu, L., and J. Gong, 2006: A study on application OIQC method to velocity dealiasing of Doppler radar VAD velocity data. *Plateau Meteor.*, **25**, 862–869.

Zittel, W. D., D. Saxion, R. Rhoton, and D. C. Crauder, 2008: Combined WSR-88D technique to reduce range aliasing using phase coding and multiple Doppler scans. *24th Conf. on Integrated Information and Processing*, New Orleans, LA, Amer. Meteor. Soc., P2.9. [Available online at https://ams.confex.com/ams/88Annual/techprogram/paper_131757.htm.]